Ab Initio Multiple Spawning Photochemical Dynamics of DMABN Using GPUs

Basile F. E. Curchod,[1,2] Aaron Sisto,[1,2] and Todd J. Martínez[1,2]

[1]Department of Chemistry and the PULSE Institute, Stanford University, Stanford, CA 94305, USA

[2]SLAC National Accelerator Laboratory, Menlo Park, CA 94025, USA

Abstract

The ultrafast decay dynamics of 4-(N,N-dimethylamino)benzonitrile (DMABN) following photoexcitation was studied with the *ab initio* multiple spawning (AIMS) method, combined with GPU-accelerated linear-response time-dependent density functional theory (LR-TDDFT). We validate the LR-TDDFT method for this case and then present a detailed analysis of the first ≈200 fs of DMABN excited-state dynamics. Almost complete nonadiabatic population transfer from S_2 (the initially populated bright state) to S_1 takes place in less than 50 fs, without significant torsion of the dimethylamino (DMA) group. Significant torsion of the DMA group is only observed after the nuclear wavepacket reaches S_1 and acquires locally-excited electronic character. Our results show that torsion of the DMA group is not prerequisite for nonadiabatic transitions in DMABN, although such motion is indeed relevant on the lowest excited state (S_1).

I. Introduction

Rarely in the field of photochemistry has an apparently simple organic molecule generated such a large number of experimental and theoretical studies as 4-(N,N-dimethylamino)-benzonitrile (scheme 1), commonly referred to as DMABN. DMABN has become a paradigmatic example for the phenomenon of *dual fluorescence*, since it fluoresces at two different energies,[1] depending on experimental conditions such as solvent polarity and temperature.[2] The locally excited (LE) band dominates the fluorescence spectra of DMABN in apolar solvent, whereas a low-energy fluorescence band, termed intramolecular charge transfer (ICT), is observed in the presence of polar solvent.
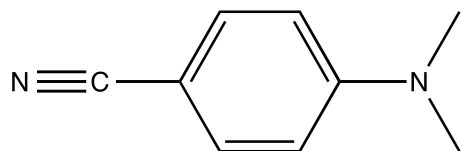
Scheme 1. 4-(N,N-dimethylamino)-benzonitrile (DMABN).

From a photophysical point of view, DMABN is expected to quickly relax in its first electronic state (S_1) after photoexcitation, where an adiabatic equilibration takes place on the picosecond timescale between two S_1 minima with differing electronic character, S_1-LE and S_1-ICT. Subtle variations in the experimental conditions directly alter the population of the different S_1 minima, engendering a large diversity of luminescence ranging from complete S_1-LE emission to complete S_1-ICT emission. The molecular geometry of the emitting charge transfer state is still controversial[3-5] and different structures have been proposed. Among them, we mention the twisted (T)-ICT by Grabowski and coworkers[6] (perhaps the most commonly accepted possibility), the planar (P)-ICT and wagging (W)-ICT by Zachariasse,[7-8] as well as the rehybridized (R)-ICT geometry[9-11] (a detailed account of the different mechanisms proposed in the literature as well as previous theoretical and experimental work on DMABN can be found in previous work[2]). The "twisting" refers to torsion of the dimethylamino (DMA) group. The DMA group is coplanar with the phenyl moiety in the electronic ground state (S_0), but twists to 90° in the S_1-ICT minimum and 150° in the S_1-LE minimum. Theory has not been able to unambiguously determine the fluorescence mechanism, although many electronic structure methods have been employed to probe the critical points of the S_1 potential energy surface in

both gas and condensed phases. Electronic structure methods used to examine the details of the emission process have included linear-response time-dependent density functional theory[12-14] (LR-TDDFT), single-reference wavefunction methods such as TDHF/CIS,[15] DFT/SCI,[16] CC2,[17] and ADC(2),[18] and multi-reference wavefunction methods such as CASSCF[19-21] and CASPT2.[22-25]

Even though a large number of experimental and theoretical data have been generated on the emission properties of DMABN and its chemical derivatives, much less information is available on the early nonadiabatic, i.e., non-Born-Oppenheimer, relaxation pathway following DMABN photoexcitation. Most theoretical and experimental studies agree that, at least in the gas phase, DMABN is initially promoted to its second excited state, which has ICT character.[13-14,20,26-29] In a gas phase multiphoton ionization experiment, Fuß and coworkers proposed that DMABN reaches the S_2/S_1 crossing in less than 100 fs (see below for more details).[29] Their analysis of the experimental data was based on the presumption that DMA twisting dominates the S_2/S_1 crossing. In contrast, theoretical calculations based on CASSCF in gas phase reported[20] that the S_2/S_1 minimum energy conical intersection (MECI) is energetically accessible with a broad range of twist angles close to 180°. Further analysis of the corresponding branching plane did not reveal any contribution from the twist angle. Subsequent CASSCF calculations with different active spaces further confused the issue, predicting conical intersection geometries ranging from a half-twisted DMA group[30] to a complete 90° twist.[21] Static calculations therefore offered a plethora of possible mechanisms, but excited-state dynamics is required to shed light on the interplay between all these different potential pathways.[24] Very recently, the first excited-state dynamics of DMABN, based on trajectory surface hopping (TSH) dynamics with ADC(2)[31] and LR-TDDFT,[32] tend to confirm that significant twisting of the DMA group is not required for nonadiabatic transitions from S_2 to S_1.

In the following, we present a detailed study of the early nonadiabatic dynamics of DMABN in the gas phase using the Ab Initio Multiple Spawning (AIMS) method, based on electronic structure properties computed with a GPU-accelerated implementation of LR-TDDFT. Derived from a rigorous formalism, AIMS accurately describes the coherent population transfer occurring in nonadiabatic regions and it has been successfully used to understand photochemical and photophysical processes of organic and inorganic molecules. We clearly identify an ultrafast deactivation pathway from the photoexcited S_2 state to the first excited electronic state S_1. The

twist angle remains close to 180° during the nonadiabatic transitions and most of the early molecular distortions involve the phenyl ring. By carefully analyzing electronic properties such as components of the transition dipole moment, we identify the electronic character describing the wavepacket dynamics of DMABN during and after the nonadiabatic transitions.

The article is organized in the following way. We begin with a short introduction to the AIMS method for nonadiabatic dynamics and proceed with a detailed section about the computational protocol and a detailed validation of the computational protocol. We then present and discuss our main results, first in the context of nonadiabatic transitions between S_2 and S_1, and then by discussing the electronic character of DMABN at different stages of the dynamics.

II. Theory

IIa. Brief summary of Full and Ab Initio Multiple Spawning

The total wavefunction for a molecular system, $\Psi(\mathbf{r},\mathbf{R},t)$, can be represented by the Born-Huang expansion,[33]

$$\Psi(\mathbf{r},\mathbf{R},t) = \sum_I \Omega_I(\mathbf{R},t)\Phi_I(\mathbf{r};\mathbf{R}), \tag{1}$$

where each $\Phi_I(\mathbf{r};\mathbf{R})$ is a fixed-nuclei solution of the time-independent Schrödinger equation for state I with corresponding electronic energy $E_I^{el}(\mathbf{R})$. In Full Multiple Spawning (FMS), the nuclear wavefunction on electronic state I is expressed as a linear combination of multidimensional frozen Gaussians called Trajectory Basis Functions (TBFs), leading to the following form of Eq. (1):[34-35]

$$\Psi(\mathbf{r},\mathbf{R},t) = \sum_I \sum_{l=1}^{N_I(t)} C_l^I(t)\chi_l^I\left(\mathbf{R};\bar{\mathbf{R}}_l^I(t),\bar{\mathbf{P}}_l^I(t),\bar{\gamma}_l^I(t),\alpha_l^I\right)\Phi_I(\mathbf{r};\mathbf{R}), \tag{2}$$

where the lth Gaussian function on the Ith electronic state is centered at position $\bar{\mathbf{R}}_l^I(t)$ and momentum $\bar{\mathbf{P}}_l^I(t)$. The phase space centers of the TBFs are evolved classically, while the width α_l^I is frozen and the phase $\bar{\gamma}_l^I(t)$ is integrated semiclassically.[36] The time-evolution of the complex coefficients $\left\{C_l^I(t)\right\}_{l=1}^{N_I(t)}$ for each electronic state I are given by the time-dependent Schrödinger equation expressed in the basis of frozen Gaussian functions. A complete discussion of the FMS equations of motion has been given previously.[36]

In Eq. (2), the number of TBFs used to describe a nuclear wavefunction in state I, $N_I(t)$, is time-dependent. This is due to the so-called spawning process, which is at the heart of the FMS method and ensures an accurate description of nonadiabatic processes by spawning new TBFs when needed, i.e., the number of TBFs describing the nuclear wavefunction on state I will grow in time. Briefly, when a TBF enters a region of strong nonadiabaticity (where the nonadiabatic coupling is large), a new TBF can be created on the coupled electronic state to ensure a proper description of the population transfer. Detailed discussions about the spawning algorithm and the different conditions leading to a spawning event have been given previously.[36-38]

In Ab Initio Multiple Spawning (AIMS),[36,38-39] the time-evolution of the TBFs is achieved by simultaneous ("on-the-fly") computation of the required electronic structure properties (such as electronic energies, gradients, and nonadiabatic coupling matrix elements). Two important numerical approximations are often employed to reduce computational effort. First, the integrals involving potential energy surfaces and nonadiabatic couplings, required in the time-evolution of the complex coefficients, are computed using the zeroth-order saddle-point approximation. Second, the initial nuclear wavefunction is represented at time $t = 0$ by a given number of initial TBFs, which are assumed to evolve independently in the subsequent nuclear dynamics (independent first generation approximation). Previous reviews have discussed both approximations.[36,40-42] It is finally important to note that the calculation of the 3N dimensional nonadiabatic coupling vectors can be computationally demanding. However, the complete nonadiabatic coupling vector becomes unnecessary whenever the zeroth-order saddle-point approximation to the coupling matrix elements is used. Instead, the projected coupling vector along the nuclear velocity vector (which has both real and imaginary parts) is used both to evaluate integrals over Gaussian functions and also to monitor the interaction between electronic states.[43] This reduces the problem of computing the full nonadiabatic coupling vectors to a simple numerical derivative along the real and imaginary parts of the nuclear velocity matrix element vector.

Nonadiabatic coupling vectors between the ground and any excited states can in principle be computed exactly from LR-TDDFT,[44-48] while couplings between excited states are only approximated in the linear-response formalism.[49] Nevertheless, it has been shown that the adiabatic approximation to LR-TDDFT (which is effectively the only practical option) cannot properly describe couplings between the first excited state and the ground state.[50-52] It has been

suggested[50] that the spin-flip variants[53] of LR-TDDFT might solve this problem, and some promising results for S_0/S_1 conical intersections have been obtained with this strategy.[54-57] Unfortunately, spin-flip LR-TDDFT often leads to severe spin contamination, which has been a stumbling block to widespread use.

In this work, we present the first application of AIMS coupled with LR-TDDFT for the calculation of electronic energies, excited-state gradients, and nonadiabatic coupling terms. The combination of LR-TDDFT and nonadiabatic dynamics has a rather long history and the interested reader is referred to previous reviews for more details.[58-60] Our focus on DMABN allows us to sidestep the formal difficulties that LR-TDDFT has with S_0/S_1 conical intersections, since the interesting nonadiabatic dynamics in this molecule involves transitions between S_2 and S_1. Of course, nonradiative transitions from S_1 to S_0 are also possible, but on a much longer (many picosecond) time scale that we do not address here.

IIb. Computational details

The nonadiabatic dynamics of DMABN was modeled with the AIMS method coupled with the DFT and LR-TDDFT implementation of the GPU-accelerated software TeraChem.[61-64] We avoid any detailed comment on the GPU acceleration of the underlying electronic structure methods here. However, we will point out that this is a significant factor in enabling us to follow the dynamics of hundreds of TBFs. Other workers have also found that GPU acceleration can be quite beneficial for electronic structure.[65-69]

The first four electronic states were considered in the dynamics (S_0, S_1, S_2, and S_3) and the required electronic structure quantities were obtained with DFT[70-71] and LR-TDDFT,[72-74] applying the Tamm-Dancoff[75-76] and the adiabatic approximation to the latter. We used the ωPBE long-range corrected exchange and correlation functional[77-79] with a range separation parameter of 0.3 bohr^{-1} and a 6-31G basis set[80] (see Sec. IId and SI for discussion and validation of the electronic structure method). Classical nuclear propagation used a time step of 20 a.u. (reduced to 5 a.u. in regions with large nonadiabatic coupling). The spawning threshold was set to 0.005 a.u.$^{-1}$ (scalar product of the nonadiabatic coupling vectors and the nuclear velocities), and the minimum TBF population required to spawn was 0.1.

A Wigner distribution for v=0 in the harmonic approximation was generated based on the ground-state geometry and corresponding frequencies. Excitation energies for the first three

excited states were then computed with LR-TDDFT/ωPBE(0.3)/6-31G based on a set of 198 randomly selected points from the constructed Wigner distribution and a photoabsorption cross-section was generated using the equation:[81-82]

$$\sigma(E) = \frac{\pi e^2}{2mc\varepsilon_0} \sum_{L \neq I}^{N_s} \left[\frac{1}{N_p^L} \sum_k^{N_p^L} f_{IL}(\mathbf{R}_k) g\left(E - \Delta E_{IL}(\mathbf{R}_k), \delta\right) \right], \tag{3}$$

where vertical excitation energies between initial state I (ground state) and state L, $\Delta E_{IL}(\mathbf{R}_k)$, and corresponding oscillator strengths, $f_{IL}(\mathbf{R}_k)$, were computed for each sampled point $\mathbf{R}_k$. N_s is the number of excited states considered, N_p^L the number of sampled points, and $g(\ldots)$ represents a normalized Lorentzian function with phenomenological broadening factor δ (=0.05 eV).

We then chose 21 different initial conditions (positions and momenta for the initial TBFs) from the 198 phase space points used to generate the absorption spectrum. These initial conditions were randomly sampled according to their oscillator strength and the constraint that their $S_0 \rightarrow S_2$ transition energy is located in a window of ±0.25 eV around the maximum of the S_2 band in the photoabsorption cross-section (5.23 eV).[83] Each initial condition was then placed on S_2 and propagated using AIMS for 8000 a.u. (192 fs).

Static DFT and LR-TDDFT calculations (geometry optimization and frequency calculations), as well as ab initio molecular dynamics simulations were all performed with TeraChem, using the same functional, basis set, and approximations as described before (unless otherwise stated). The Turbomole software,[84-86] version 6.4, was used for the excited-state calculations based on the correlated single-reference wavefunction-based methods ADC(2)[87-90] and for ground-state MP2 calculations.[91] We also employed the CC2 method[92] for some validation benchmarks. These ADC(2)/MP2/CC2 calculations used a TZVPP[93] or a cc-pVTZ[94] basis set and employed both the resolution of the identity[91] and frozen core approximations. Frequency calculations were performed for all optimized geometries to confirm that they correspond to a minimum on the corresponding potential energy surface. Molecular representations were generated with VMD.[95]

IIc. Simulation analysis

As described in Sec. IIa, the overall AIMS/LR-TDDFT nonadiabatic dynamics consists of a series of independent AIMS runs, starting from different initial conditions (nuclear geometries and momenta). Each of these runs starts with a single initial TBF, in state S_2, which can spawn

additional TBFs whenever a region of strong nonadiabaticity is visited. In those particular regions, the nuclear timestep is reduced from that in uncoupled regions.

The overall population of the different electronic states is computed from an incoherent average over the population obtained from the 21 AIMS runs. For each of these runs, the population is obtained coherently. This leads to the following equation for the final population $P_I(t)$ of state I at time t:

$$P_I(t) = \frac{1}{N_{runs}} \sum_{M=1}^{N_{runs}} \left[\sum_{k,l}^{N_I(t)} C_{k,M}^{I*}(t) C_{l,M}^{I}(t) S_{kl,M}^{II} \right]. \tag{3}$$

where $S_{kl,M}^{II}$ represents an overlap integral between TBFs k and l, both evolving on electronic state I, for the AIMS run M. As a technical point, we note that TBFs have different lengths of time, since they may be created by spawning from other TBFs throughout the dynamics. It also happens that a TBF, on rare occasions, may be discarded if its population falls below a given threshold (< 0.1) and if it is not coupled to any other TBFs (i.e., the off-diagonal matrix element of the Hamiltonian between this TBF and any other is negligibly small). This discarding of negligibly-populated, uncoupled TBFs minimizes unnecessary computational expense. The process of analyzing the data is simplified if all TBFs are placed on a common time grid by using linear interpolation, and we assume this has been done in the discussion below.

To calculate any property $\bar{O}(t)$ of interest, the following equation is used:

$$\bar{O}(t) = \frac{1}{N_{runs}} \sum_{M}^{N_{runs}} \left[\frac{\sum_{k}^{N_{TBF}^M(t)} C_{k,M}^{*}(t) C_{k,M}(t) O\left(\bar{\mathbf{R}}_{k,M}(t)\right)}{\sum_{k}^{N_{TBF}^M(t)} C_{k,M}^{*}(t) C_{k,M}(t)} \right], \tag{4}$$

where t is time (a point on the common time grid of interpolated data), and $N_{TBF}^M(t)$ is the total number of TBFs at time t in a given run M. The value of the property evaluated at the position $\bar{\mathbf{R}}_{k,M}(t)$ of TBF k at time t in the AIMS run M is denoted as $O\left(\bar{\mathbf{R}}_{k,M}(t)\right)$. Some examples of properties $\bar{O}(t)$ that might be computed include twist angles or bond lengths. In this work, we will use the following definition[96] for the pyramidalization angle of a given TBF at nitrogen atom N13 (atom labeling refers to Table 1):

$$O_{k,M}^{\mathrm{pyr,N13}}(t) = \arccos\left(\left(\mathbf{e}_{\mathrm{N13-C18}}^{k,M}(t) \times \mathbf{e}_{\mathrm{N13-C14}}^{k,M}(t)\right) \cdot \mathbf{e}_{\mathrm{N13-C4}}^{k,M}(t)\right) - \frac{\pi}{2}, \tag{5}$$
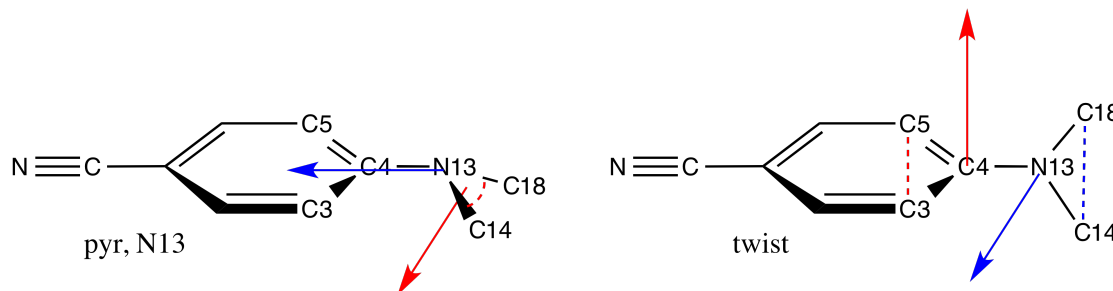
where $\mathbf{e}_{A-B}^{k,M}(t) = \dfrac{\mathbf{R}_A^{k,M}(t) - \mathbf{R}_B^{k,M}(t)}{\left\| \mathbf{R}_A^{k,M}(t) - \mathbf{R}_B^{k,M}(t) \right\|}$ represents a unit vector pointing from atom A to atom B at

time t. The twist angle of the DMA group[97] is computed as:

$$O_{k,M}^{twist}(t) = \left(\mathbf{e}_{C4-N13}^{k,M}(t) \times \mathbf{e}_{C5-C3}^{k,M}(t) \right) \cdot \left(\mathbf{e}_{N13-C4}^{k,M}(t) \times \mathbf{e}_{C18-C14}^{k,M}(t) \right). \tag{6}$$

Scheme 2 provides a graphical representation of the pyramidalization and twist angle.

Scheme 2. Definition of the pyramidalization of N13 (left) and twist (right). The red (blue) arrow represents the left (right) side of the dot product in each respective equation.

Finally, the time-resolved emission spectra were obtained from the equation[98]

$$O_{k,M}^{emi}(E,t) = \left| \boldsymbol{\mu}\left(\overline{\mathbf{R}}_{k,M}(t) \right) \right|^2 \left(\frac{1}{\sigma \sqrt{2\pi}} \exp\left(-\frac{\left(E - \Delta E\left(\overline{\mathbf{R}}_{k,M}(t) \right) \right)}{2\sigma^2} \right) \right), \tag{7}$$

where $\boldsymbol{\mu}\left(\overline{\mathbf{R}}_{k,M}(t) \right)$ and $\Delta E\left(\overline{\mathbf{R}}_{k,M}(t) \right)$ represent the transition dipole moment and the energy gap

between the ground state and the electronic state associated with TBF k at time t in run M (σ is a

broadening parameter set to 0.212 eV).

IId. Validation of the computational protocol

LR-TDDFT can be an efficient and accurate method for the calculation of electronic excited state

energies and properties, but there can also be problems.[51,99] We have already discussed the

difficulties arising from the adiabatic approximation (neglecting frequency dependence of the

exchange correlation kernel). Further difficulties can arise with commonly used functionals such

as gradient-corrected GGAs or hybrid functionals like B3LYP. DMABN constitutes a striking

example[12] of the failure of GGA/hybrid LR-TDDFT to reproduce electronic states with

pronounced charge-transfer character.[100] These problems can often be alleviated with long-range

exact exchange, i.e. range-separated hybrids.[77,79,101] Indeed, range-separated hybrids do lead to

potential energy scans in good agreement with single-reference wavefunction-based methods for

DMABN.[12,14] Here we comment on validation of LR-TDDFT/ωPBE by comparison to the single-reference wavefunction methods CC2 and ADC(2) for different molecular geometries of DMABN.

DFT and LR-TDDFT/ωPBE optimized geometries in S_0 and in S_1 are in rather good agreement with those obtained with ADC(2) (Table 1) and similar trends are observed when comparing S_0 and S_1 structures. We note that ADC(2) structures are similar to the ones reported for CC2 with the same basis set.[17] Interestingly, the ground-state geometry obtained with DFT/ωPBE/6-31G is completely flat, in agreement with the result from other long-range corrected functionals[14] (small variations of the wagging angle however seem to only slightly affect the electronic energy of the different states[16]). The twist of the DMA group is near zero at the ground-state geometry (ground-state ab initio molecular dynamics at 300K shows that this twist angle only slightly deviates from planarity, see Figure S4). As noted in previous studies[12,14] and in comparison to CC2 or ADC(2), LR-TDDFT with long-range corrected functionals tends to overestimate the transition energies in the Franck-Condon region. However, the energy gap between S_2 and S_1 at the ground-state geometry is in better agreement between the two methods (0.27 eV for ADC(2) and 0.40 eV for LR-TDDFT/ωPBE).

An important difference between ADC(2) and LR-TDDFT/ωPBE for DMABN is the relative stability of the S_1-LE and S_1-(T)ICT excited state minima. Both ADC(2) and LR-TDDFT/ωPBE indicate that S_1-(T)ICT is lower in energy than S_1-LE in the gas phase (see also Ref.[18]), but LR-TDDFT predicts a larger stability difference. In fact, high-level wavefunction methods suggest that the correct ordering is reversed, i.e. the S_1-LE minimum should be more stable than the S_1-(T)ICT minimum in the gas phase[17,24] (this stability is reversed in polar solvents). These differences are most important for strongly twisted molecules and are not expected to affect the qualitative behavior of the S_2/S_1 nonadiabatic dynamics. Because of the uncertainties in this respect, we do not attempt to simulate the long time S_1 adiabatic dynamics of DMABN in gas phase (see below).

To further validate the adequacy of LR-TDDFT/ωPBE for the nonadiabatic dynamics of interest, we computed excitation energies along a rigid scan of the DMA twist using different methods (Figure S1). The portion of the LR-TDDFT/ωPBE scan corresponding to near planar twist angles is nearly parallel to the equivalent curves computed with ADC(2) or CC2. We also

compared CC2 and LR-TDDFT electronic energies at different geometries extracted from AIMS/LR-TDDFT/ωPBE dynamics evolving on S_2 (Figure S2). This comparison shows that LR-TDDFT and CC2 produce nearly parallel electronic energy curves even far from the Franck-Condon region. Based on the same geometries, we further validated that the simple 6-31G basis set is adequate to simulate the low-lying electronic states of DMABN by comparison with 6-31G* (Figure S3). Past studies have also noted that a rather small basis set already provides a qualitatively correct description of DMABN electronic states.[16,102]

Finally, the accuracy of LR-TDDFT/ωPBE to describe the excited-state dynamics of DMABN is indirectly verified by the similarity of our results (presented below) with those

Table 1. Comparison between LR-TDDFT/TDA/ωPBE(ω=0.3)/6-31G and ADC(2)/TZVPP for the ground-state, S_1-LE, and S_1-(T)ICT optimized geometries. ΔE^{el} indicates an electronic energy difference with respect to the S_1-LE optimized geometry. Energies are given in eV, bond lengths in Å, and angles in degrees. Atom numbering is indicated in the structure below. Absorption/emission energies are for $S_0 \rightarrow S_2$ and $S_1 \rightarrow S_0$ transitions, respectively.

|	C2-C3 (C5-C6)	C1-C7	C7-N8	C4-N13	Wagging N	Twist	ΔE^{el}	Abs./Emis. (f_{osc})
S_0								
ωPBE	1.388	1.433	1.174	1.381	0.0	179.9	0.55	5.36 (0.7654)
ADC(2)	1.386	1.428	1.173	1.379	23.1	180.0	0.57	4.69 (0.5522)
S_1-LE								
ωPBE	1.428 (1.429)	1.432	1.175	1.391	-0.7	156.3	0.00	4.52 (0.0344)
ADC(2)	1.439 (1.436)	1.428	1.174	1.389	-1.4	159.8	0.00	3.74 (0.0299)
S_1-(T)ICT								
ωPBE	1.371	1.417	1.180	1.421	0.4	89.9	-0.66	3.02 (0.0004)
ADC(2)	1.371	1.409	1.182	1.443	0.0	90.0	-0.15	2.44 (0.0007)
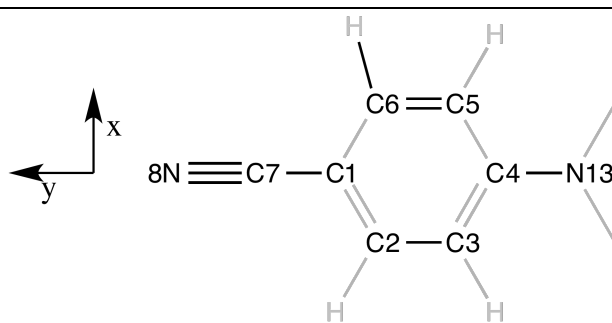
reported in recent theoretical work[31] based on TSH dynamics and ADC(2) for the electronic structure. A more extended discussion can be found below.

III. Results and Discussion: Ab Initio Multiple Spawning Simulation of DMABN

The UV/Vis portion of the computed photoabsorption spectra for DMABN (Figure 1) is dominated by a transition from the ground state to the second excited state (S_2), the latter being of intramolecular charge transfer (ICT) character. The electronic excitation between S_0 and S_1 (locally excited state, LE) is only weakly allowed and forms a shoulder on the low-energy side of the bright $S_0 \rightarrow S_2$ transition. The overall shape and width of the photoabsorption spectra reproduces qualitatively the experimental vapor-phase absorption spectra obtained at 150°C (Figure S5). To gain insight into the character of the electronic transitions, Figure 2 depicts a density difference plot for both $S_0 \rightarrow S_1$ and $S_0 \rightarrow S_2$ transitions, at the ground-state optimized geometry. The electronic density is depleted around the nitrogen atom of the DMA group in both cases, while the increase in density is observed mostly on the phenyl ring for the LE state and on both the phenyl ring and the cyano group for the ICT state.

In agreement with previous studies,[14,29,103] these observations point towards a major population of the S_2 state upon photoexcitation of DMABN at the absorption maximum of the lowest energy band. We therefore initiate the AIMS dynamics on S_2 for 21 initial conditions (the corresponding spectra and molecular structures are shown in Figure 1). We first present the relaxation dynamics in terms of adiabatic electronic states, S_1 and S_2, and we then discuss the electronic character of the molecule during excited-state dynamics.

As shown in Figure 3, AIMS/LR-TDDFT dynamics predicts a rapid decay from S_2 (L_a, in Platt notation) to S_1 (L_b). As a result of the close energetic proximity of S_2 and S_1 in the Franck-Condon region, population transfer begins quickly (within a few femtoseconds) and depletes 50% of the S_2 population within 11 fs. After 46 fs, the S_2 contribution to the total wavepacket has fallen to 20%. The S_3 state is weakly populated (< 4%), and this population is depleted within 35 fs. Interestingly, there is also a weak repopulation of S_2 after 125 fs. Spawning of new TBFs lies at the heart of the AIMS method, and this is clearly illustrated by the dark grey dashed line in Figure 3 that reports on the number of TBFs as a function of time. The nuclear wavepacket is described at time t=0 by 21 uncoupled TBFs, and each of them will spawn (and become coupled with) new TBFs whenever a nonadiabatic region is encountered during the dynamics. As a result,
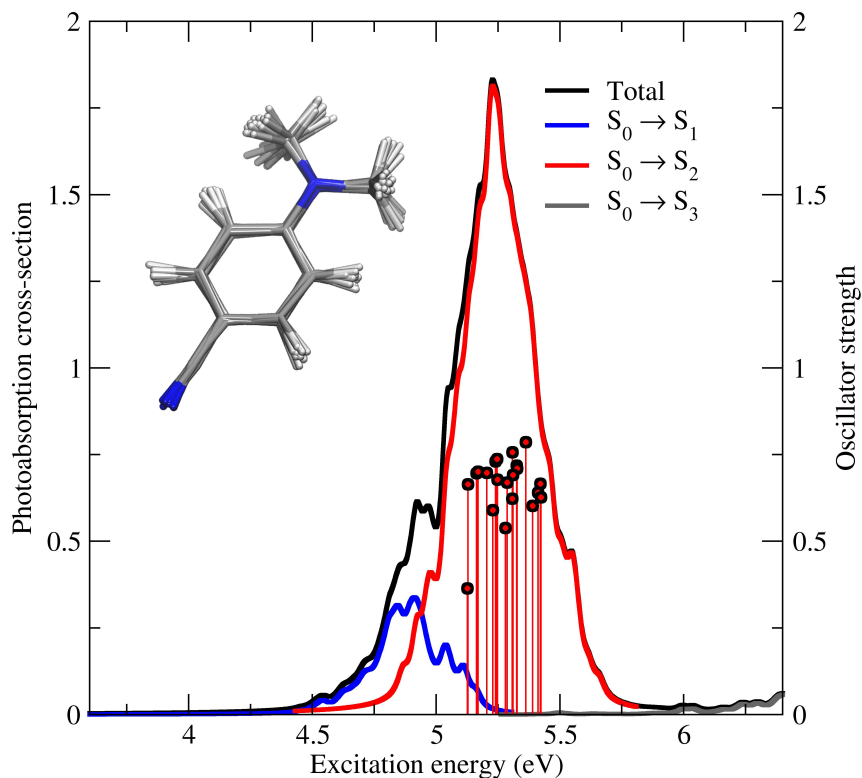
Figure 1. Photoabsorption cross-section (black line, in Å^{-2}) for the first three transitions of DMABN, based on 198 configurations sampled from a Wigner distribution. The different contributions are given in blue ($S_0 \rightarrow S_1$), red ($S_0 \rightarrow S_2$), and gray ($S_0 \rightarrow S_3$). Sticks with circles highlight the geometries chosen for the initial conditions of the AIMS/LR-TDDFT dynamics (heights correspond to oscillator strength and corresponding molecular geometries are depicted in the inset).
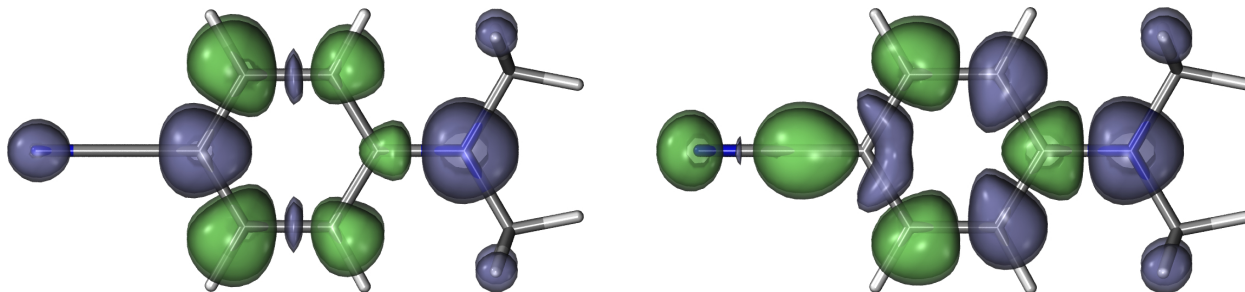
Figure 2. Density difference plots for the S_1-LE (left) and S_2-ICT (right) states of DMABN, at the ground-state optimized geometry. (ice blue: $\Delta\rho<0$, lime green: $\Delta\rho>0$. Isovalue=0.00001).

the overall number of running trajectories increases to 186 by the end of the simulation (192 fs).

It is of interest to characterize the degree to which conical intersections play a role in the observed nonadiabatic transitions. In Figure 4, we show the amount of population transfer from S_2 to S_1 as a function of the S_2/S_1 electronic energy gap at the spawning geometry. Most of the population transfer indeed occurs very close to conical intersections, i.e. at small energy gaps

less than 0.1 eV. However, weak population transfer is observed for gaps as large as 0.4 eV. This is in line with previous reports[104-105] showing that the "reach" of the conical intersection can be quite long.

Often, minimal energy conical intersections (MECIs) are located and used in order to characterize nonadiabatic decay mechanisms. Thus, it is also of interest to determine the dynamic relevance of these geometries. In the inset of Figure 4, we show the amount of $S_2 \rightarrow S_1$ population transfer as a function of the energy above the planar S_2/S_1 MECI in DMABN. Interestingly, the majority of the population transfer occurs quite far from the MECI (average of approximately 2 eV above the MECI), at least as judged from an energetic perspective. No population transfer is observed for molecular geometries within 1 eV of the MECI. This is also in line with previous reports in other molecules[104-105] and suggests that MECIs need not be dominant in excited state dynamics. This is a consequence of the rather large dimensionality of the intersection seam and the non-equilibrium nature of excited state dynamics. We note that in DMABN, there are two S_2/S_1 MECIs of possible importance (see Figure S11). One of these is planar and the DMA group is twisted relative to the phenyl ring in the other. In Figure 4, we are comparing the energy of geometries where transitions occur to the planar S_2/S_1 MECI, which is actually the less stable of the two. Thus, a comparison to the lowest energy MECI would accentuate even further the point that MECI geometries are of limited relevance in the dynamics (because the average energy above the MECI for geometries promoting nonadiabatic transitions would be even larger than what is shown in Figure 4.) As we have previously discussed,[104] MECI geometries can be useful as "signposts" on the potential energy surfaces, even if dynamical transitions occur at configurations which are quite distorted variants. We also note that solvent-induced dissipation effects is not expected to play a major role in the S_2 to S_1 decay since this decay is both ultrafast and dominated by small amplitude motion. Thus, a similar picture for Fig. 4 would be expected in solvent. It will be interesting to test this in future work with excited state dynamics simulations including solvent.

An important feature of DMABN photophysics is the potential interplay between twisting angle and electronic state couplings. AIMS/LR-TDDFT indicates that the ultrafast decay from S_2 to S_1 is not directly correlated with a 90° twist of the DMA moiety (left panel of Figure 5), as the average twist angle for the initial condition TBFs on S_2 changes by less than 20° during the first 50 fs of dynamics (when the nonadiabatic transitions from S_2 to S_1 occur). This observation is
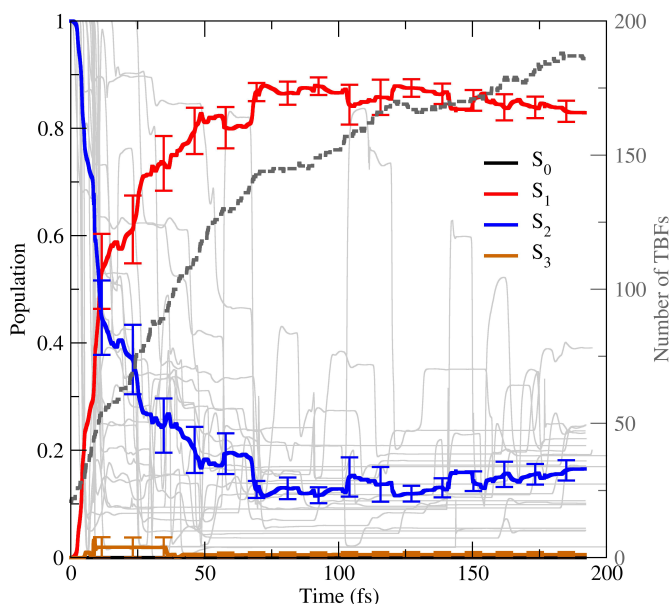
Figure 3. Population of the different electronic states considered in the AIMS dynamics of DMABN, averaged over 21 ICs. The dashed gray line represents the total number of TBFs running at a given time t over the full AIMS dynamics. Thin gray lines give the S_2 population along each individual AIMS runs.
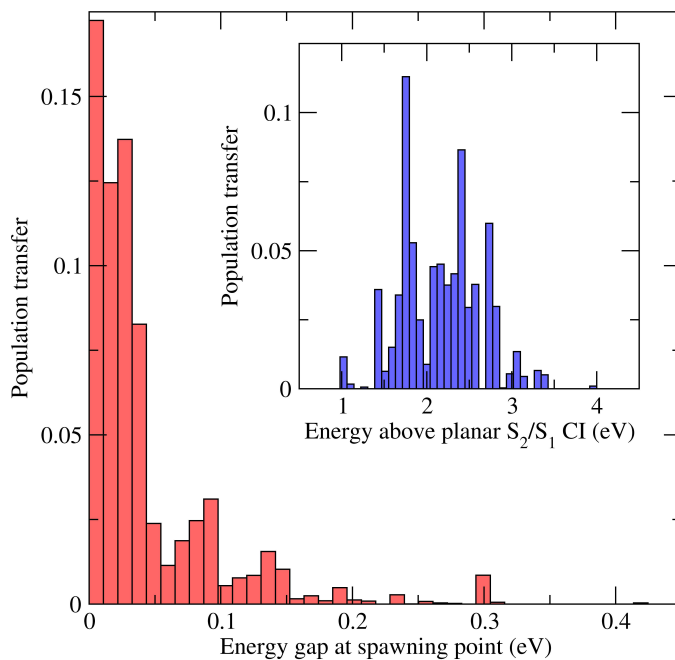
Figure 4. Histograms showing the correlation between energy gap and population transfer for each S_2/S_1 spawning event during the complete AIMS dynamics. The population transfer is defined as the sum, over all S_2/S_1 spawning events, of the population gained by the child TBF from the beginning of the coupled propagation until the step following the spawning point, normalized by the total number of AIMS runs. The inset shows a histogram of the population transfer as a function of the energy difference between the spawning TBF and the optimized planar S_2/S_1 minimum energy conical intersection.

further confirmed by the inspection of the spawning geometries between S_2 and S_1 (inset of the left panel of Figure 5), which consistently show an average twist angle of 173.7°. We note that the spawning geometries for upward transitions from S_1 to S_2 look rather similar, with a slightly smaller average twist angle of 168.4°, as shown in the inset of the right panel of Figure 5. The near-planar structures that dominate the initial S_2/S_1 nonadiabatic transitions resemble a planar S_2/S_1 MECI ("pCI" in Figure S11) that we have located. As mentioned above, a lower energy S_2/S_1 MECI exists, where the DMA group is twisted relative to the phenyl ring by approximately 54° ("tCI" in Figure S11). The DMA group does twist somewhat during the dynamics, which is expected since both the S_1-LE and S_1-(T)ICT minima are partially twisted (see Table 1). However, this twisting is far from a complete 90° twist in the first 200 fs following photoexcitation (such a large twisting was expected by much of the early theoretical and experimental work).

In the right panel of Figure 5, we show the DMA torsional dynamics for the entire set of TBFs (the initial conditions on S_2 and all the spawned TBFs on S_1 or S_2). The width of the lines is proportional to the population of the corresponding TBF. One can see that there is negligible torsion in the first 50fs. Over the entire course of the dynamics, only a few TBFs twist by as
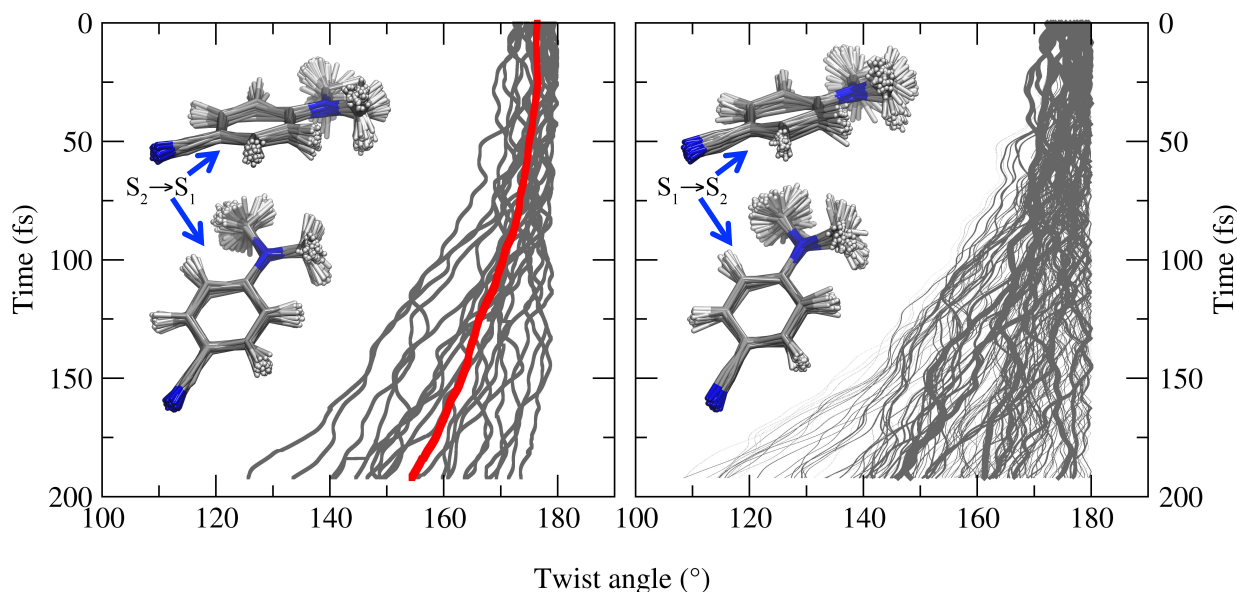

Figure 5. Twist angle of the DMA group during the AIMS dynamics of DMABN, after photoexcitation to S_2. Left panel: Twisting angle averaged over 21 ICs. Red=average; grey=incoherent summation over the TBFs generated by each individual IC. The different spawning geometries for transitions from S_2 to S_1 are represented in the inset. Right panel: twist angle for the complete swarm of TBFs. The line width is proportional to the TBF population. The different spawning geometries for transitions from S_1 to S_2 are represented in the inset.

much as 65°, but these also carry relatively little population. Most of the population is twisted by less than 40° (twist angles greater than 140° in Figure 5) after 200fs of dynamics.

Analyzing other geometrical parameters during the dynamics, we observe that the central phenyl C-C bonds (C2-C3 and C5-C6) elongate quickly in response to the change in electronic configuration (Figure 6, lower right panel). Interestingly, the C2-C3 and C5-C6 bond lengths stabilize around a value characteristic of the equilibrium C-C bond length at the S_1-LE optimized geometry (Figure 6, orange line), indicating that a large portion of the nuclear wavepacket acquires a S_1-LE character ($\pi\pi^*$ character located on the benzene moiety). We note in addition that the oscillations of these two benzene C-C bonds evolve first in phase for 50 fs of dynamics and then out-of-phase. Other bond lengths are not strikingly altered during the nonadiabatic dynamics, even if the C4-N13 bond (of the DMA group) seems to expand slightly (upper right panel of Figure 6), as expected from Table 1. Furthermore, only a moderate pyramidalization occurs around the DMA group in the first 200 fs of dynamics (Figure S6). The latter observation is further confirmed by a moderate average N13 pyramidalization angle of 7.7° for the S_2/S_1
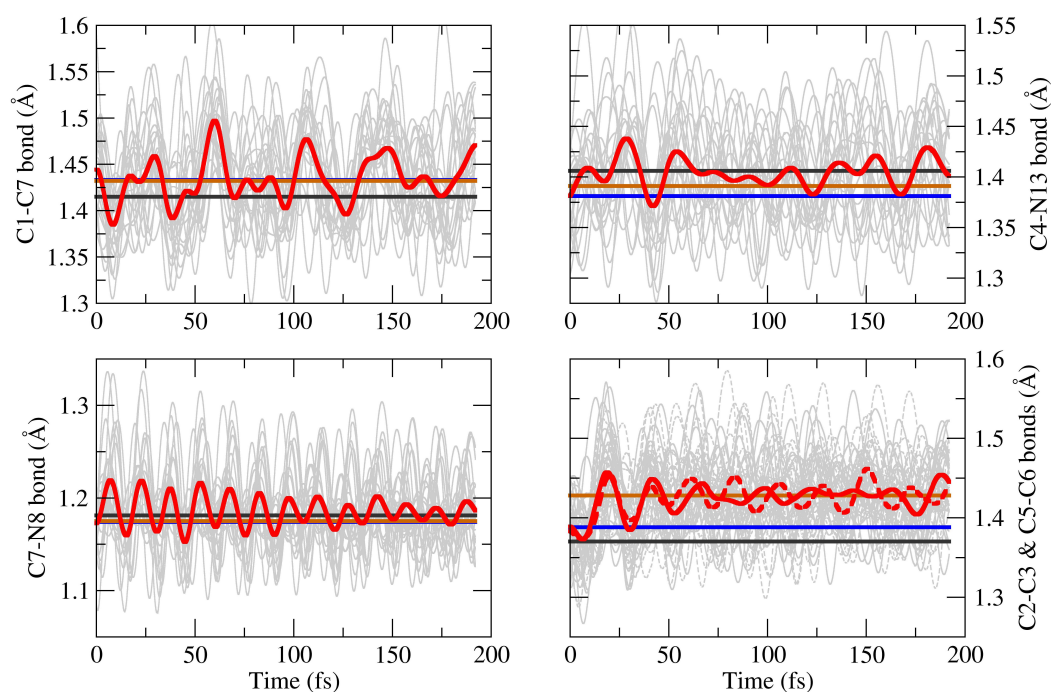
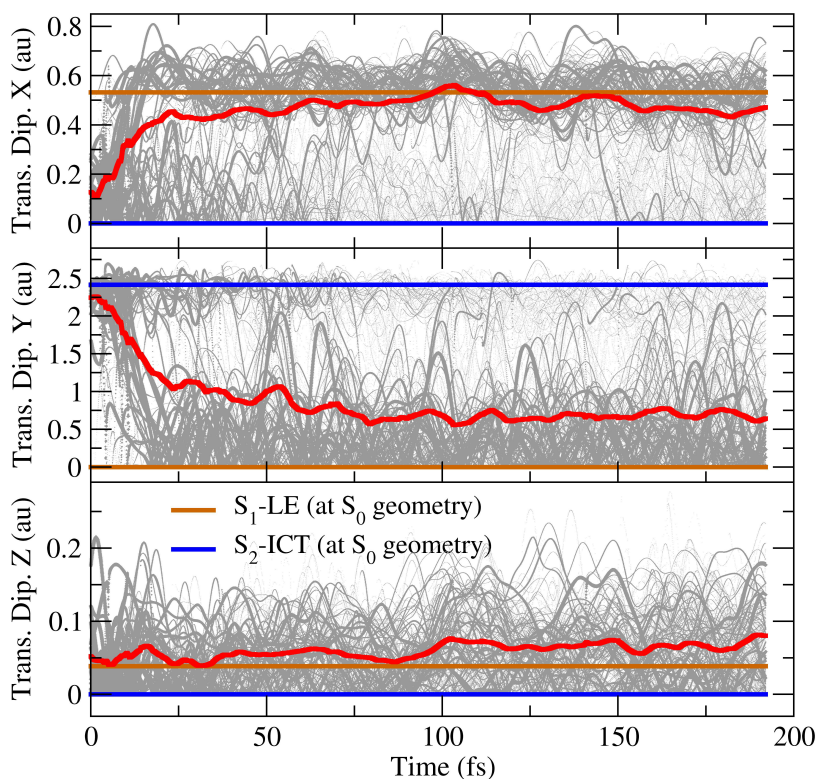**Figure 6**. Bond lengths during the AIMS dynamics of DMABN, initiated in S_2. Red=average over 21 ICs; light grey=incoherent summation over the TBFs generated by each individual IC. Blue line: bond length at ground-state optimized geometry; gray line: bond length at S_1-LE optimized geometry; green line: bond length at S_1-(T)ICT optimized geometry. Atom numbering refers to the structure presented in Table 1.

spawning trajectories (inset of left panel in Figure 5). In their theoretical study,[20] Robb et al. further discussed the possibility for DMABN to relax into a (R)ICT state (rehybridized internal charge transfer state) in S_1. This character is obtained when the carbon of the cyano group changes its hybridization from *sp* to *sp*^{2}, resulting in a bent cyano group (C1-C7-N8 angle of 122° at the minimum). However, no C-C-N bending is observed in the AIMS dynamics, although the average value for ∠CCN deviates slightly from linearity (Figure S7).

Up to this point, the main observation is that DMABN relaxes from S_2 to S_1 within 50 fs, with no significant twist of the DMA group. The evolution of the bond lengths is consistent with LE electronic character once the molecule reaches S_1. Further quantification of the electronic character after relaxation would be desirable. The transition dipole moments are ideal for this, since their components can be used as markers for LE/ICT character of the electronic state (Figure 7). At the ground-state geometry, sizeable X and Z components (aligned on the short molecular axis, see structure in Table 1) characterize the transition dipole moment between S_0 and S_1-LE state, while the Y component is close to zero. On the other hand, the Y component of the transition dipole moment (aligned on the long molecular axis, see structure in Table 1) between S_0 and S_2-ICT is large for the ICT state, whereas both X and Z components are small. (A similar trend is observed for the transition dipole moments at the S_1-LE relaxed geometry.) Therefore, the transition dipole moment components, averaged over the 21 AIMS runs, can be used as a tracer for the electronic character of the AIMS wavepacket along the nonadiabatic dynamics.[106] In the first few femtoseconds of dynamics, the molecule exhibits as expected a large transition dipole moment along the long (Y) axis (Figure 7, middle panel), characteristic of S_2-ICT and almost matching the value computed for the S_2-ICT state at the ground-state optimized geometry. The Y component of the wavepacket transition dipole rapidly drops and the X component rises, matching the S_2 population decay (Figure 3) and indicating a change in the electronic character from ICT to LE. This alteration in the electronic character is however not complete and a limited portion of the nuclear wavepacket still exhibits some ICT character, as indicated by the gray lines in Figure 7. These lines represent the transition dipole moment values for each TBF of the AIMS dynamics, while their thicknesses are proportional to the TBF population. Figure 7 shows that most of the wavepacket evolves towards LE character within the first 50 fs after photoexcitation, but a small number of TBFs oscillate between ICT and LE

character. Interestingly, and consistent with our observation, a mixed contribution of long- and short-axis fluorescence was observed experimentally.[29]

Figure 7. Components of the transition dipole moment during the AIMS dynamics of DMABN after $S_0 \rightarrow S_2$ photoexcitation. Red line shows the incoherent summation of each component of the transition dipole moment over the TBFs generated by each individual IC, averaged over the 21 AIMS runs. Each gray line represents the transition dipole moment value for a given TBF of the swarm and the line thickness is proportional to the population of this TBF. Orange thick line: value of the transition dipole moment for S_1-LE, at the ground-state geometry. Blue thick line: value of the transition dipole moment for S_2-ICT, at the ground-state geometry.

In Figure 8, we report the AIMS-predicted time-resolved fluorescence spectrum, averaged over the 21 AIMS runs. This spectrum further highlights the rapid decay from the bright S_2 (ICT) state into the darker S_1 state with a dominant LE character, accompanied by a Stokes shift of almost 1 eV. At longer time ($t > 100$ fs), the emission energy drifts to somewhat lower energy. Experimentally, the gap between the absorption band and the S_1-LE emission is ~0.7 eV in THF[107] and ~1 eV in vapor phase.[108] The femtosecond time-resolved fluorescence spectrum of DMABN has yet to be measured.
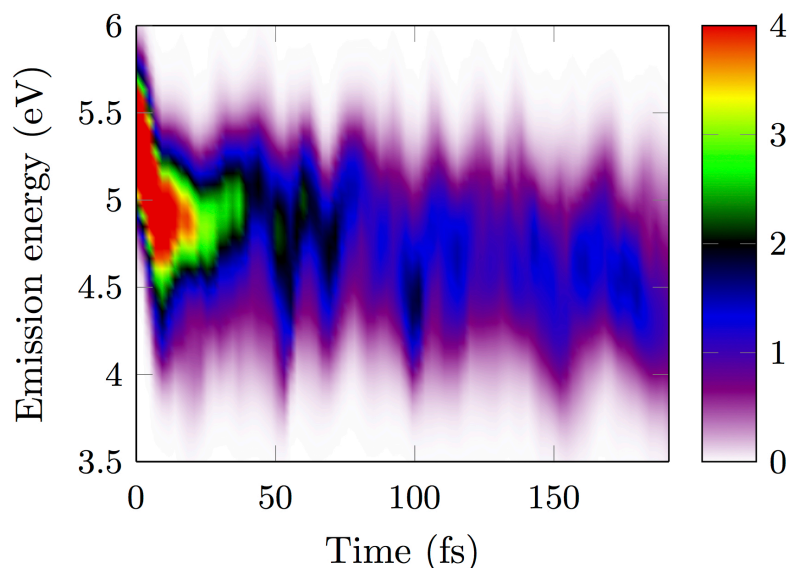
Figure 8. Time-resolved emission spectra of DMABN averaged over the 21 AIMS runs (intensity units are arbitrary).

The results discussed so far corroborate Robb's proposal[20] and recent observations[24,31-32] that DMABN does not necessarily need a large twist of the DMA group to relax from S_2 to S_1 (and further shows that large scale twisting is not only unnecessary but also does not occur). The branching plane of the S_2/S_1 conical intersection (determined with CASSCF) is mostly formed by nuclear displacement of the phenyl ring and C-N stretch. The AIMS/LR-TDDFT dynamics confirms the rapid change in phenyl ring bond length. The initial photoexcited state has ICT character, and this quickly switches to LE character (as confirmed by transition dipole moments in Figure 7) within 50 fs. This switch of electronic character happens in concert with $S_2 \rightarrow S_1$ nonadiabatic transitions. However, the switch from ICT to LE character is not complete and both electronic characters are present during the first 100 fs after photoexcitation.

Fuß et al. reported a relaxation time of 68 fs for DMABN in gas phase.[29,109] This relaxation time in gas phase comprises two components: $\tau_1=5\pm5$ fs, interpreted as the time needed to leave the Frank-Condon region, and $\tau_2=63\pm7$ fs, corresponding to the time for a relaxation in LE (L_b) or CT. As discussed in Ref. [31], the initial interpretation of the experimental lifetime is based on the assumption that DMABN requires a twist of the DMA group to reach the S_2/S_1 crossing region.[29] Fuß et al. proposed that an increase in the fragmentation of DMABN should be related to variation of a large amplitude nuclear motion.[29] In a subsequent article,[28] the mechanism of the initial relaxation is further clarified: the authors proposed that τ_1 is related to the departure

from the Franck-Condon region *via* a quinoidal distortion of the benzene ring, while τ_2 is the time needed for the wavepacket to travel through the conical intersection with both twisting and arching motion of the DMA group. According to our simulations, the S_2/S_1 transfer happens almost immediately after photoexcitation to S_2 and 50% of the S_2 population is transferred to S_1 in 10.6 fs. A fit by two exponentials of the S_2 decay in the first 75 fs gives a short and a long component of 9.1 fs and 82.8 fs respectively, in good agreement with the timescales observed experimentally. In the early stage of the dynamics, only the bond lengths in the phenyl ring show sizeable variations. Importantly, these particular phenyl bond stretches constitute the dominant contributions to the nonadiabatic coupling vectors computed between S_2(CT) and S_1(LE) using EOM-CCSD or LR-TDDFT (see Ref. [31] and Figure S10), which are also in qualitative agreement with results from CASSCF.[20] The twist of the DMA group starts to decrease only after 30 fs of dynamics. τ_1 could therefore be related to the ultrafast decay of the wavepacket in S_2, correlated with the initial relaxation of geometrical coordinates in the phenyl ring, in agreement with the experimental interpretation as the time required to leave the Franck-Condon region.[28] (We note that also experimental studies of DMABN in solvent mentioned the importance of the quinoidal stretching vibration for the S_2/S_1 relaxation.[26]) On the other hand and in agreement with Ref. [31], τ_2 could potentially correspond to the time required for the twist angle to reach its equilibrium value after relaxation in S_1, i.e., a significantly different value from the one observed in the Franck-Condon region. As already mentioned in previous paragraphs, the ultrafast S_2/S_1 nonadiabatic dynamics produced by AIMS/LR-TDDFT matches the results of recent theoretical studies by Miller et al[31] and Lan et al,[32] as does the smooth and weak population exchange between S_1 and S_2 observed after 125 fs and the weak population of S_3. The conclusions of the aforementioned studies are that significant DMA twisting is not required for the S_2/S_1 radiationless transition to take place and that in the early stage of the nonadiabatic dynamics, the pyramidalization coordinate fluctuates around what corresponds to a near-planar geometry. Importantly, the study reported in Ref. [31] used a different nonadiabatic scheme, TSH vs. AIMS, and a different electronic structure method, ADC(2) vs. LR-TDDFT. The close agreement with our results despite the different theoretical approaches is therefore reassuring and strengthens the conclusion of both works. It is nevertheless important to stress that while AIMS represents a clear improvement over TSH, both ADC(2) and LR-TDDFT might suffer from the lack of multireference character. However, a recent article based on static calculations at the

multireference configuration interaction (MRCI) level of theory confirmed that the S_2/S_1 branching space does not contain DMA torsion.[110] In addition, the multireference results are consistent with ultrafast S_2/S_1 decay occurring *via* mostly planar geometries, as observed in our work and in Ref. [31].

We close with a comment about the electronic structure methods used. Previous studies have recognized that CC2, ADC(2), and LR-TDDFT underestimate the energy of the gas phase S_1-(T)ICT minimum, placing it at a lower energy than the S_1-LE minimum. Long-time dynamics with these methods will therefore tend to overestimate the population reaching the S_1-(T)ICT minimum, preventing accurate analysis of the adiabatic reaction taking place between S_1-LE and S_1-(T)ICT. While the difference in energy between the two S_1 minima is rather small with CC2 and ADC(2), it becomes larger within LR-TDDFT/ωPBE(0.3), as shown in Table 1. This last point is crucial for explaining the behavior of DMABN at longer (>1 ps) timescale and to address the question of the molecular geometry leading to fluorescence. Results from adiabatic ab initio molecular dynamics on S_1 are reported in the supporting material (Figure S9), initialized from the last step of a well-populated AIMS trajectory basis function evolving on S_1. As expected and in agreement with Ref. [31], DMABN rapidly and adiabatically visits regions in configuration space close to the S_1-(T)ICT minimum, i.e., with a twist angle of nearly 90 degrees. However, given that multireference correlated wavefunction methods (expected to be more accurate than single reference methods such as CC2, ADC(2) or LR-TDDFT) predict the ordering with the S_1-LE minimum more stable than the S_1-(T)ICT minimum,[24,110] this result should be interpreted with great care.

IV. Summary and Conclusion

Ab initio multiple spawning, combined for the first time with a GPU-accelerated implementation of LR-TDDFT, was used to shed light on the early-stage nonadiabatic dynamics of DMABN in the gas phase. In line with other theoretical studies, we showed clear evidence of ultrafast nonadiabatic decay from S_2 to S_1 in DMABN. The S_2/S_1 population transfer is not directly correlated with the twist of the DMA group, but rather most of the nonadiabatic transitions occur while the molecule is still nearly planar. Twisting of the DMA group does occur, but only after the wavepacket is relaxing on S_1. The timescale of DMA twisting matches the measured experimental lifetime quite well. According to our gas phase calculations, the

nuclear wavepacket acquires a dominant LE character within the first 25 fs after photoexcitation. However, a realistic picture of the long-time adiabatic equilibration on S_1 would require an electronic structure method capable of accurately describing the relative energies of the S_1-LE and S_1-ICT minima. The LR-TDDFT method overstabilizes the S_1-ICT minimum and thus we did not follow the long time dynamics here. Future work should address the role of solvent in state ordering and crossings to determine how solvent affects the nonadiabatic decay mechanism.

V. Acknowledgments

VI. Supporting Information Available.
Detailed comparisons of torsional energy scans and critical point energies from wavefunction and density functional methods with different basis sets. Comparison of experimental and LR-TDDFT electronic absorption spectra. Time evolution of geometric parameters. The Supporting Information is available free of charge on the ACS Publications website.

TOC Graphic
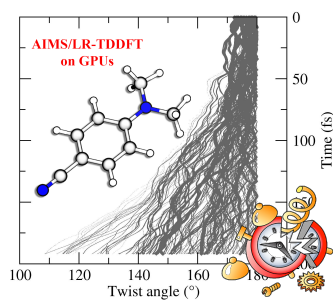
References

1. Lippert, E.; Lüder, W.; Moll, F.; Nägele, W.; Boos, H.; Prigge, H.; Seibold-Blankenstein, I., Umwandlung von Elektronenanregungsenergie. *Ang. Chem.* **1961,** *73*, 695-706.

2. Grabowski, Z. R.; Rotkiewicz, K.; Rettig, W., Structural changes accompanying intramolecular electron transfer: focus on twisted intramolecular charge-transfer states and structures. *Chem. Rev.* **2003,** *103*, 3899-4032.

3. Zachariasse, K. A., Comment on "On the dual emission of p-dimethylaminobenzonitrile and its photophysical implications". *Phys. Chem. Chem. Phys.* **2013,** *15*, 16976-16977.

4. Catalan, J., On the dual emission of p-dimethylaminobenzonitrile and its photophysical implications. *Phys. Chem. Chem. Phys.* **2013,** *15*, 8811-8820.

5. Catalan, J., Reply to the comment on "On the dual emission of p-dimethylaminobenzonitrile and its photophysical implications" by J. Catalan, Phys. Chem. Chem. Phys., 2013, 15, 8811-8820. *Phys. Chem. Chem. Phys.* **2013,** *15*, 16978-16979.

6. Rotkiewicz, K.; Grellman, K. H.; Grabowski, Z. R., Reinterpretation of Anomalous Fluorescence of "Para-N,N-Dimethylamino-Benzonitrile. *Chem. Phys. Lett.* **1973,** *19*, 315-318.

7. Zachariasse, K. A.; Grobys, M.; vonderHaar, T.; Hebecker, A.; Ilichev, Y. V.; Morawski, O.; Ruckert, I.; Kuhnle, W., Photoinduced intramolecular charge transfer and internal conversion in molecules with a small energy gap between S-1 and S-2. Dynamics and structure. *J. Photochem. Photobio. A* **1997,** *105*, 373-383.

8. Schuddeboom, W.; Jonker, S. A.; Warman, J. M.; Leinhos, U.; Kuhnle, W.; Zachariasse, K. A., Excited-State Dipole-Moments of Dual Fluorescent 4-(Dialkylamino)Benzonitriles - Influence of Alkyl Chain-Length and Effective Solvent Polarity. *J. Phys. Chem.* **1992,** *96*, 10809-10819.

9. Lewis, F. D.; Holman, B., Singlet-States of Benzonitrile and Para-Dimethylaminobenzonitrile. *J. Phys. Chem.* **1980,** *84*, 2326-2328.

10. Sobolewski, A. L.; Domcke, W., Charge transfer in aminobenzonitriles: Do they twist? *Chem. Phys. Lett.* **1996,** *250*, 428-436.

11. Sobolewski, A. L.; Domcke, W., Promotion of intramolecular charge transfer in dimethylamino derivatives: Twisting versus acceptor-group rehybridization. *Chem. Phys. Lett.* **1996,** *259*, 119-127.

12. Wiggins, P.; Williams, J. A. G.; Tozer, D. J., Excited state surfaces in density functional theory: A new twist on an old problem. *J. Chem. Phys.* **2009,** *131*, 091101.

13. Rappoport, D.; Furche, F., Photoinduced intramolecular charge transfer in 4-(dimethyl)aminobenzonitrile--a theoretical perspective. *J. Amer. Chem. Soc.* **2004,** *126*, 1277-1284.

14. Chiba, M.; Tsuneda, T.; Hirao, K., Long-range corrected time-dependent density functional study on fluorescence of 4,4'-dimethylaminobenzonitrile. *J. Chem. Phys.* **2007,** *126*, 034504.

15. Mennucci, B.; Toniolo, A.; Tomasi, J., Ab initio study of the electronic excited states in 4-(N, N-dimethylamino) benzonitrile with inclusion of solvent effects: the internal charge transfer process. *J. Amer. Chem. Soc.* **2000,** *122*, 10621-10630.

16. Parusel, A. B. J.; Kohler, G.; Grimme, S., Density functional study of excited charge transfer state formation in 4-(N,N-dimethylamino)benzonitrile. *J. Phys. Chem. A* **1998,** *102*, 6297-6306.

17. Köhn, A.; Hättig, C., On the nature of the low-lying singlet states of 4-(dimethyl-amino) benzonitrile. *J. Amer. Chem. Soc.* **2004,** *126*, 7399-7410.

18. Lunkenheimer, B.; Kohn, A., Solvent Effects on Electronically Excited States Using the Conductor-Like Screening Model and the Second-Order Correlated Method ADC(2). *J. Chem. Theo. Comp.* **2013,** *9*, 977-994.

19. Cogan, S.; Zilberg, S.; Haas, Y., The electronic origin of the dual fluorescence in donor-acceptor substituted benzene derivatives. *J. Amer. Chem. Soc.* **2006,** *128*, 3335-3345.

20. Gómez, I.; Reguero, M.; Boggio-Pasqua, M.; Robb, M. A., Intramolecular charge transfer in 4-aminobenzonitriles does not necessarily need the twist. *J. Amer. Chem. Soc.* **2005,** *127*, 7119-7129.

21. Amatatsu, Y., Theoretical study on the photochemical behavior of 4-(dimethylamino)benzonitrile. *J. Phys. Chem. A* **2005,** *109*, 7225-7235.

22. Galvan, I. F.; Martin, M. E.; Aguilar, M. A., On the absorption properties of the excited states of DMABN. *Chem. Phys. Lett.* **2010,** *499*, 100-102.

23. Galvan, I. F.; Martin, M. E.; Aguilar, M. A., Theoretical Study of the Dual Fluorescence of 4-(N,N-Dimethylamino)benzonitrile in Solution. *J. Chem. Theo. Comp.* **2010,** *6*, 2445-2454.

24. Gómez, I.; Castro, P. J.; Reguero, M., Insight into the Mechanisms of Luminescence of Aminobenzonitrile and Dimethylaminobenzonitrile in Polar Solvents. An ab Initio Study. *J. Phys. Chem. A* **2015,** *119*, 1983-1995.

25. Serrano-Andres, L.; Merchan, M.; Roos, B. O.; Lindh, R., Theoretical-Study of the Internal Charge-Transfer in Aminobenzonitriles. *J. Amer. Chem. Soc.* **1995,** *117*, 3189-3204.

26. Rhinehart, J. M.; Mehlenbacher, R. D.; McCamant, D., Probing the Charge Transfer Reaction Coordinate of 4-(Dimethylamino)benzonitrile with Femtosecond Stimulated Raman Spectroscopy. *J. Phys. Chem. B* **2010,** *114*, 14646-14656.

27. Lee, J.-K.; Fujiwara, T.; Kofron, W. G.; Zgierski, M. Z.; Lim, E. C., The low-lying pi-sigma* state and its role in the intramolecular charge transfer of aminobenzonitriles and aminobenzethyne. *J. Chem. Phys.* **2008,** *128*, 164512.

28. Fuß, W.; Schmid, W. E.; Pushpa, K. K.; Trushin, S. A.; Yatsuhashi, T., Ultrafast relaxation and coherent oscillations in aminobenzonitriles in the gas phase probed by intense-field ionization. *Phys. Chem. Chem. Phys.* **2007,** *9*, 1151-1169.

29. Fuß, W.; Pushpa, K. K.; Rettig, W.; Schmid, W. E.; Trushin, S. A., Ultrafast charge transfer via a conical intersection in dimethylaminobenzonitrile. *Photochem. Photobio. Sci.* **2002,** *1*, 255-262.

30. Xu, X. F.; Cao, Z. X.; Zhang, Q. N., Theoretical study of photoinduced singlet and triplet excited states of 4-dimethylaminobenzonitrile and its derivatives. *J. Chem. Phys.* **2005,** *122*, 194305.

31. Kochman, M. A.; Tajti, A.; Morrison, C. A.; Dwayne Miller, R. J., Early events in the nonadiabatic relaxation dynamics of 4-(N,N-dimethylamino)benzonitrile. *J. Chem. Theo. Comp.* **2015,** *11*, 1118-1128.

32. Du, L.; Lan, Z., An on-the-fly surface-hopping program JADE for nonadiabatic molecular dynamics of poly-atomic systems: implementation and applications. *J. Chem. Theo. Comp.* **2015,** *11*, 1360-1374.

33. Born, M.; Huang, K., *Dynamical Theory of Crystal Lattices*. Clarendon, Oxford: 1954.

34. Martínez, T. J.; Ben-Nun, M.; Levine, R. D., Multi-electronic-state molecular dynamics: A wave function approach with applications. *J. Phys. Chem.* **1996,** *100*, 7884-7895.

35. Ben-Nun, M.; Martínez, T. J., Nonadiabatic molecular dynamics: Validation of the multiple spawning method for a multidimensional problem. *J. Chem. Phys.* **1998,** *108*, 7244-7257.

36. Ben-Nun, M.; Martínez, T. J., Ab Initio Quantum Molecular Dynamics. *Adv. Chem. Phys.* **2002,** *121*, 439-512.

37. Yang, S.; Coe, J. D.; Kaduk, B.; Martínez, T. J., An "optimal" spawning algorithm for adaptive basis set expansion in nonadiabatic dynamics. *J. Chem. Phys.* **2009,** *130*, 134113.

38. Yang, S.; Martínez, T. J., Ab Initio Multiple Spawning: First Principles Dynamics Around Conical Intersections. In *Conical Intersections: Theory, Computation and Experiment*, Domcke, W.; Yarkony, D. R.; Köppel, H., Eds. World Scientific: 2011; Vol. 17, pp 347-374.

39. Ben-Nun, M.; Quenneville, J.; Martínez, T. J., Ab initio multiple spawning: Photochemistry from first principles quantum molecular dynamics. *J. Phys. Chem. A* **2000,** *104*, 5161-5175.

40. Sulc, M.; Hernandez, H.; Martínez, T. J.; Vanicek, J., Relation of exact Gaussian basis methods to the dephasing representation: Theory and application to time-resolved electronic spectra. *J. Chem. Phys.* **2013,** *139*, 034112.

41. Martínez, T. J.; Levine, R. D., Non-adiabatic molecular dynamics: Split-operator multiple spawning with applications to photodissociation. *J. Chem. Soc., Faraday Trans.* **1997,** *93*, 941-947.

42. Persico, M.; Granucci, G., An overview of nonadiabatic dynamics simulations methods, with focus on the direct approach versus the fitting of potential energy surfaces. *Theor. Chem. Acc.* **2014,** *133*, 1526.

43. Tao, H.; Levine, B. G.; Martínez, T. J., Ab initio multiple spawning dynamics using multi-state second-order perturbation theory. *J. Chem. Phys. A* **2009,** *113*, 13656-13662.

44. Chernyak, V.; Mukamel, S., Density-matrix representation of nonadiabatic couplings in time-dependent density functional (TDDFT) theories. *J. Chem. Phys.* **2000,** *112*, 3572-3579.

45. Send, R.; Furche, F., First-order nonadiabatic couplings from time-dependent hybrid density functional response theory: Consistent formalism, implementation, and performance. *J. Chem. Phys.* **2010,** *132*, 044107.

46. Hu, C.; Hirai, H.; Sugino, O., Nonadiabatic couplings from time-dependent density functional theory: Formulation in the Casida formalism and practical scheme within modified linear response. *J. Chem. Phys.* **2007,** *127*, 064103.

47. Tavernelli, I.; Curchod, B. F. E.; Rothlisberger, U., On nonadiabatic coupling vectors in time-dependent density functional theory. *J. Chem. Phys.* **2009,** *131*, 196101.

48. Tavernelli, I.; Tapavicza, E.; Rothlisberger, U., Nonadiabatic coupling vectors within linear response time-dependent density functional theory. *J. Chem. Phys.* **2009,** *130*, 124107.

49. Tavernelli, I.; Curchod, B. F. E.; Laktionov, A.; Rothlisberger, U., Nonadiabatic coupling vectors for excited states within time-dependent density functional theory and beyond. *J. Chem. Phys.* **2010,** *133*, 194104.

50. Levine, B. G.; Ko, C.; Quenneville, J.; Martínez, T. J., Conical intersections and double excitations in density functional theory. *Mol. Phys.* **2006,** *104*, 1039-1051.

51. Ullrich, C. A., *Time-Dependent Density-Functional Theory*. Oxford University Press: 2012.

52. Casida, M. E.; Huix-Rotllant, M., Many-Body Perturbation Theory (MBPT) and Time-Dependent Density-Functional Theory (TD-DFT): MBPT Insights About What Is Missing In, and Corrections To, the TD-DFT Adiabatic Approximation. In *Density-Functional Methods for Excited States*, Ferré, N.; Filatov, M.; Huix-Rotllant, M., Eds. Springer: Heidelberg, 2016; pp 1-60.

53. Shao, Y.; Head-Gordon, M.; Krylov, A. I., The spin-flip approach within time-dependent density functional theory: Theory and applications to diradicals. *J. Chem. Phys.* **2003,** *118*, 4807-4818.

54. Minezawa, N.; Gordon, M. S., Optimizing Conical Intersections by Spin−Flip Density Functional Theory: Application to Ethylene. *J. Phys. Chem. A* **2009,** *113*, 12749-12753.

55. Minezawa, N.; Gordon, M. S., Photoisomerization of stilbene: A spin-flip density functional approach. *J. Phys. Chem. A* **2011,** *115*, 7901-7911.

56. Minezawa, N.; Gordon, M. S., Optimizing conical intersections of solvated molecules: The combined spin-flip density functional theory/effective fragment potential method. *J. Chem. Phys.* **2012,** *137*, 034116.

57. Harabuchi, Y.; Keipert, K.; Zahariev, F.; Taketsugu, T.; Gordon, M. S., Dynamics simulations with spin-flip time-dependent density functional theory: Photisomerization and photocyclization mechanisms of cis-stilbene in pipi* states. *J. Phys. Chem. A* **2014,** *118*, 11987-11998.

58. Curchod, B. F. E.; Rothlisberger, U.; Tavernelli, I., Trajectory-Based Nonadiabatic Dynamics with Time-Dependent Density Functional Theory. *ChemPhysChem* **2013,** *14*, 1314-1340.

59. Tapavicza, E.; Bellchambers, G. D.; Vincent, J. C.; Furche, F., Ab initio non-adiabatic molecular dynamics. *Phys. Chem. Chem. Phys.* **2013,** *15*, 18336-18348.

60. Barbatti, M.; Crespo-Otero, R., Surface Hopping Dynamics with DFT Excited States. *Top. Curr. Chem.* **2015,** *368*, 415-444.

61. Ufimtsev, I. S.; Martínez, T. J., Quantum Chemistry on Graphical Processing Units. 3. Analytical Energy Gradients, Geometry Optimization, and First Principles Molecular Dynamics. *J. Chem. Theo. Comp.* **2009,** *5*, 2619-2628.

62. Ufimtsev, I. S.; Martínez, T. J., Quantum chemistry on graphical processing units. 1. Strategies for two-electron integral evaluation. *J. Chem. Theo. Comp.* **2008,** *4*, 222-231.

63. Ufimtsev, I. S.; Martínez, T. J., Quantum Chemistry on Graphical Processing Units. 2. Direct Self-Consistent-Field (SCF) Implementation. *J. Chem. Theo. Comp.* **2009,** *5*, 3138-3138.

64. Isborn, C. M.; Luehr, N.; Ufimtsev, I. S.; Martínez, T. J., Excited-State Electronic Structure with Configuration Interaction Singles and Tamm--Dancoff Time-Dependent Density Functional Theory on Graphical Processing Units. *J. Chem. Theo. Comp.* **2011,** *7*, 1814-1823.

65. Yasuda, K., Two-electron integral evaluation on the graphics processor unit. *J. Comp. Chem.* **2008,** *29*, 334-342.

66. Asadchev, A.; Allada, V.; Felder, J.; Bode, B. M.; Gordon, M. S.; Windus, T. L., Uncontracted Rys quadrature implementation of up to G functions on graphical processing units. *J. Chem. Theo. Comp.* **2010,** *6*, 696-704.

67. Asadchev, A.; Gordon, M. S., Mixed precision evaluation of two-electron integrals by Rys quadrature. *Comp. Phys. Comm.* **2012,** *183*, 1563-1567.

68. Asadchev, A.; Gordon, M. S., New multithreaded hybrid CPU/GPU approach to Hartree-Fock. *J. Chem. Theo. Comp.* **2012,** *8*, 4166-4176.

69. Yasuda, K., Accelerating density functional calculations with graphics processing unit. *J. Chem. Theo. Comp.* **2008,** *4*, 1230-1236.

70. Hohenberg, P.; Kohn, W., Inhomogeneous electron gas. *Phys. Rev. B* **1964,** *136*, B864-B871.

71. Kohn, W.; Sham, L. J., Self-consistent equations including exchange and correlation effects. *Phys. Rev.* **1965,** *140*, A1133-A1138.

72. Runge, E.; Gross, E. K. U., Density-functional theory for time-dependent systems. *Phys. Rev. Lett.* **1984,** *52*, 997-1000.

73. Casida, M. E., Time-dependent density-functional response theory for molecules. In *Recent Advances in Density Functional Methods*, Chong, D. P., Ed. Singapore, World Scientific: 1995; p 155.

74. Petersilka, M.; Gossmann, U. J.; Gross, E. K. U., Excitation Energies from Time-Dependent Density-Functional Theory. *Phys. Rev. Lett.* **1996,** *76*, 1212-1215.

75. Tamm, I., *J. Phys. (Moscow)* **1945,** *9*, 449.

76. Dancoff, S. M., Non-Adiabatic Meson Theory of Nuclear Forces. *Phys. Rev.* **1950,** *78*, 382-385.

77. Tawada, Y.; Tsuneda, T.; Yanagisawa, S.; Yanai, T.; Hirao, K., A long-range-corrected time-dependent density functional theory. *J. Chem. Phys.* **2004,** *120*, 8425-8433.

78. Vydrov, O. A.; Heyd, J.; Krukau, A. V.; Scuseria, G. E., Importance of short-range versus long-range Hartree-Fock exchange for the performance of hybrid density functionals. *J. Chem. Phys.* **2006,** *125*, 074106.

79. Vydrov, O. A.; Scuseria, G. E., Assessment of a long-range corrected hybrid functional. *J. Chem. Phys.* **2006,** *125*, 234109.

80. Ditchfield, R.; Hehre, W. J.; Pople, J. A., Self-Consistent Molecular-Orbital Methods .9. Extended Gaussian-Type Basis for Molecular-Orbital Studies of Organic Molecules. *J. Chem. Phys.* **1971,** *54*, 724-728.

81. Barbatti, M.; Aquino, A. J. A.; Lischka, H., The UV absorption of nucleobases: semi-classical ab initio spectra simulations. *Phys. Chem. Chem. Phys.* **2010,** *12*, 4959-4967.

82. Bergsma, J. P.; Berens, P. H.; Wilson, K. R.; Fredkin, D. R.; Heller, E. J., Electronic-Spectra from Molecular-Dynamics - a Simple Approach. *J. Phys. Chem.* **1984,** *88*, 612-619.

83. Barbatti, M.; Granucci, G.; Persico, M.; Ruckenbauer, M.; Vazdar, M.; Eckert-Maksic, M.; Lischka, H., The on-the-fly surface-hopping program system Newton-X: Application to ab initio simulation of the nonadiabatic photodynamics of benchmark systems. *J. Photochem. Photobiol. A* **2007,** *190*, 228-240.

84. Furche, F.; Ahlrichs, R.; Hattig, C.; Klopper, W.; Sierka, M.; Weigend, F., Turbomole. *WIREs: Comp. Mol. Sci.* **2014,** *4*, 91-100.

85. TURBOMOLE *TURBOMOLE*, V6.6; University of Karlsruhe and Forschungszentrum Karlsruhe GmbH, 1989-2007, TURBOMOLE GmbH, since 2007, 2014.

86. Ahlrichs, R.; Bar, M.; Haser, M.; Horn, H.; Kolmel, C., Electronic-structure calculations on workstation computers - the program system TURBOMOLE. *Chem. Phys. Lett.* **1989,** *162*, 165-169.

87. Schirmer, J., Beyond the Random-Phase Approximation - a New Approximation Scheme for the Polarization Propagator. *Phys Rev A* **1982,** *26*, 2395-2416.

88. Trofimov, A. B.; Schirmer, J., An Efficient Polarization Propagator Approach to Valence Electron-Excitation Spectra. *J Phys B-at Mol Opt* **1995,** *28*, 2299-2324.

89. Dreuw, A.; Wormit, M., The algebraic diagrammatic construction scheme for the polarization propagator for the calculation of excited states. *WIREs: Comp. Mol. Sci.* **2015,** *5*, 82-95.

90. Hattig, C., Structure optimizations for excited states with correlated second-order methods: CC2 and ADC(2). *Adv. Quantum Chem.* **2005,** *50*, 37-60.

91. Hättig, C.; Weigend, F., CC2 excitation energy calculations on large molecules using the resolution of the identity approximation. *J. Chem. Phys.* **2000,** *113*, 5154-5161.

92. Christiansen, O.; Koch, H.; Jorgensen, P., The second-order approximate coupled cluster singles and doubles model CC2. *Chem. Phys. Lett.* **1995,** *243*, 409-418.

93. Weigend, F.; Häser, M.; Patzelt, H.; Ahlrichs, R., RI-MP2: optimized auxiliary basis sets and demonstration of efficiency. *Chem. Phys. Lett.* **1998,** *294*, 143-152.

94. Weigend, F.; Köhn, A.; Hättig, C., Efficient Use of the Correlation Consistent Basis Sets in Resolution of the Identity MP2 Calculations. *J. Chem. Phys.* **2002,** *116*, 3175-.

95. Humphrey, W.; Dalke, A.; Schulten, K., VMD -- Visual Molecular Dynamics. *J. Mol. Graph.* **1996,** *14*, 33-38.

96. Lee, A. M. D.; Coe, J. D.; Ullrich, S.; Ho, M. L.; Lee, S. J.; Cheng, B. M.; Zgierski, M. Z.; Chen, I. C.; Martínez, T. J.; Stolow, A., Substituent effects on dynamics at conical intersections: alpha,beta-enones. *J. Phys. Chem. A* **2007,** *111*, 11948-11960.

97. Mori, T.; Glover, W. J.; Schuurman, M. S.; Martínez, T. J., Role of Rydberg States in the Photochemical Dynamics of Ethylene. *J. Phys. Chem. A* **2012,** *116*, 2808-2818.

98. Coe, J. D.; Levine, B. G.; Martínez, T. J., Ab initio molecular dynamics of excited-state intramolecular proton transfer using multireference perturbation theory. *J. Phys. Chem. A* **2007,** *111*, 11302-11310.

99. Casida, M. E.; Huix-Rotllant, M., Progress in Time-Dependent Density-Functional Theory. *Ann. Rev. Phys. Chem.* **2012,** *63*, 287-323.

100. Dreuw, A.; Weisman, J. L.; Head-Gordon, M., Long-range charge-transfer excited states in time-dependent density functional theory require non-local exchange. *J. Chem. Phys.* **2003,** *119*, 2943-2946.

101. Peach, M. J. G.; Benfield, P.; Helgaker, T.; Tozer, D. J., Excitation energies in density functional theory: An evaluation and a diagnostic test. *J. Chem. Phys.* **2008,** *128*, 044118.

102. Cammi, R.; Mennucci, B.; Tomasi, J., Fast evaluation of geometries and properties of excited molecules in solution: a Tamm-Dancoff model with application to 4-dimethylaminobenzonitrile. *J. Phys. Chem. A* **2000,** *104*, 5631-5637.

103. Worth, G.; Robb, M.; Burghardt, I., A novel algorithm for non-adiabatic direct dynamics using variational Gaussian wavepackets. *Faraday Disc.* **2004,** *127*, 307-323.

104. Levine, B. G.; Martínez, T. J., Isomerization through conical intersections. *Ann. Rev. Phys. Chem.* **2007,** *58*, 613-634.

105. Coe, J. D.; Ong, M. T.; Levine, B. G.; Martínez, T. J., On the Extent and Connectivity of Conical Intersection Seams and the Effects of Three-State Intersections. *J. Phys. Chem. A* **2008,** *112*, 12559-12567.

106. For each TBF in a given AIMS run, the transition dipole moment used corresponds to a transition between the ground state and the electronic state which the TBF is associated with. The results are then incoherently averaged according to Eq. 5 to get the red line in Figure 7.

107. Park, M.; Im, D.; Rhee, Y. H.; Joo, T., Coherent and Homogeneous Intramolecular Charge-Transfer Dynamics of 1-tert-Butyl-6-cyano-1,2,3,4-tetrahydroquinoline (NTC6), a Rigid Analogue of DMABN. *J. Phys. Chem. A* **2014,** *118*, 5125-5134.

108. Daum, R.; Druzhinin, S.; Ernst, D.; Rupp, L.; Schroeder, J.; Zachariasse, K. A., Fluorescence excitation spectra of jet-cooled 4-(diisopropylamino)benzonitrile and related compounds. *Chem. Phys. Lett.* **2001,** *341*, 272-278.

109. Trushin, S. A.; Yatsuhashi, T.; Fuss, W.; Schmid, W. E., Coherent oscillations in the charge-transfer system 4-dimethylamino-benzonitrile. *Chem. Phys. Lett.* **2003,** *376*, 282-291.

110. Georgieva, I.; Aquino, A. J.; Plasser, F.; Trendafilova, N.; Kohn, A.; Lischka, H., Intramolecular Charge-Transfer Excited-State Processes in 4-(N,N-Dimethylamino)benzonitrile: The Role of Twisting and the pisigma* State. *J. Phys. Chem. A* **2015,** *119*, 6232-6243.